Radius and chirality dependence of the radial breathing mode and the *G*-band phonon modes of single-walled carbon nanotubes

Valentin N. Popov* and Philippe Lambin

Laboratoire de Physique du Solide, Facultés Universitaires Notre-Dame de la Paix, Rue de Bruxelles 61, B-5000 Namur, Belgium

The radial breathing and *G*-band vibrational modes of all 300 single-walled carbon nanotubes in the radius range from 2 to 12 Å were calculated within a symmetry-adapted nonorthogonal tight-binding model. The dynamical matrix was calculated within this model using the linear-response approximation. The obtained phonon frequencies show well-expressed radius and chirality dependence and family behavior. The curvature-induced effects on the frequencies are found to be important for small- and moderate-radius tubes. The strong electron-phonon interactions in metallic tubes bring about Kohn anomalies of certain phonon branches. Among the Raman-active phonons, these interactions have strongest effect on the longitudinal tangential A_1 phonons of metallic tubes, whose frequency becomes lower than that of the transverse tangential A_1 phonons. The calculated frequencies are compared to available theoretical and experimental data.

PACS number(s): 61.46.−w, 63.22.+m, 73.22.−f, 78.67.Ch

I. INTRODUCTION

The vibrational and electronic properties of carbon nanotubes have amazing peculiarities originating from the quasi-one-dimensionality of these systems.[1] The carbon nanotubes are synthesized in a large variety of structures. Some of them consist of a single cylindrical graphitic layer, so-called single-walled nanotubes. Others comprise a number of co-axial layers, so-called multiwalled nanotubes. The nanotubes often stick together in bundles. In both cases, the separate carbon layers are coupled together by weak van der Waals interactions. Therefore, the main object for the study of the vibrational and electronic properties of the nanotubes is the isolated single-walled nanotubes (later on referred to simply as the nanotube). The effect of the interlayer interactions on these properties can be accounted for by using the theory of perturbations. The theoretical predictions of these properties can be applied directly for the purposes of the structural characterization of the produced nanotubes. In particular, the Raman scattering measurements on nanotube samples reveal that the spectra are dominated by a low-frequency band $(100–450 \text{ cm}^{-1})$ and a high-frequency band $(1500–1650 \text{ cm}^{-1})$. The former originates from a vibrational mode with uniform radial atomic displacements [the so-called radial-breathing mode (RBM)]. The frequency of this mode is roughly inversely proportional to the nanotube diameter[2–4] with small deviations from this law depending on chirality, intertube interactions, and interactions with the environment.

The higher-frequency band (so-called *G* band) arises from six tangential bond-stretching vibrational modes of symmetries $2A_1$, $2E_1$, and $2E_2$ (see, e.g., Ref. 5). This band is usually observed as two subbands: a G^+ subband with almost tube-independent frequency and a G^- subband with decreasing frequency with the decrease of the tube radius.[6] In an early theoretical work on phonons in nanotubes[3] it was stated that the tangential modes have either longitudinal optical (LO) or transverse optical (TO) character with respect to the tube axis. Later on, it was argued that these modes are only approximately longitudinal and transverse.[7] It was proven

that for the *G*-band frequencies holds that $A_1^{LO} > A_1^{TO}$, $E_1^{LO} < E_1^{TO}$, and $E_2^{LO} < E_2^{TO}$ but the order of the three pairs of frequencies depends on the particular model.[8] It was argued that the strong electron-longitudinal optical phonon interaction in metallic tubes results in softening of the A_1^{TO} mode frequency leading to the appearance of a subband with a broad and asymmetric lineshape in the lower-frequency shoulder of the G^- subband.[9] In imperfect tubes, the latter subband is often observed to widen and shift with the laser excitation energy that was explained with double-resonance processes in nanotubes.[10] Due to the complexity of the processes giving rise to the *G* band, this band has not been used so far and possibly cannot be used for detailed structural characterization of the nanotube samples.

The theoretical work on the phonon dispersion of nanotubes has so far been limited to calculations within a force-constant model using the zone-folding method[2] or for the folded tube structure.[3,4] The calculations for all tubes of practical interest were made possible within the symmetry-adapted scheme incorporated in a force-constant lattice-dynamical model for nanotubes.[4] However, this model has the disadvantage of using force constants extracted from fittings to experimental data on graphite and therefore these constants may not describe the tube curvature effects well. Another possibility is to obtain the phonon dispersion from empirical tight-binding models,[11–13] *ab initio* models[14–16] using the supercell method, and *ab initio* models[17,18] using the perturbation technique. The tight-binding models generally overestimate the bond-stretching phonon branches by 5–10 %. The reasons for this are the incomplete atomic basis set used and the approximate description of part of the electron-electron interactions by pair potentials. The *ab initio* results overestimate the experimental data by about 1%. In all cases, the calculations were limited to achiral tubes and to a few chiral ones. The only known to the authors symmetry-adapted *ab initio* code[19] has not been used for phonon calculations. The reasons for this are possibly the intractably large supercells needed to calculate the force-constant matrix in most cases and/or the necessity to add a linear-response

module to the code for the direct evaluation of the dynamical matrix. An implementation of the symmetry-adapted scheme exists for the nonorthogonal tight-binding (NTB) model.[20] This model allows for the easy incorporation of the linear-response module and large-scale phonon calculations for nanotubes. It is therefore tempting to accomplish calculations of the zone-center phonons for all tubes of practical interest and to reveal the radius and chiral-angle dependence of the most important of them: the RBM and the *G*-band phonons.

Here we present the results for the radius and chiral-angle dependence of the RBM and the *G*-band modes of a large number of nanotubes obtained within a symmetry-adapted NTB model.[20,21] First, the tight-binding approach to the lattice dynamics of nanotubes is presented (Sec. II). In Sec. III, the results for the phonon dispersion of graphene are discussed in comparison with available experimental and theoretical data. In Sec. IV, the phonon dispersion of three nanotubes is presented and the effect of the strong electron-phonon interaction on the longitudinal tangential A_1 modes is discussed. The dependence of the frequencies of the mentioned zone-center phonons on the tube radius and chiral angle is derived. It is shown that the zone-folding method fails to reproduce this dependence fairly well for narrow up to moderate-radius tubes, in which case, the use of the nanotube structure for phonon calculations is mandatory. The paper ends up with conclusions.

II. THEORETICAL PART

A. The ideal nanotube structure

The ideal nanotube is a cylindrical structure consisting from sp^2 bound carbon atoms as in graphene. It can be viewed as obtained by cutting an infinite strip of graphene perpendicular to the lattice vector $\mathbf{C}_h = L_1\mathbf{a}_1 + L_2\mathbf{a}_2$ through its beginning and end, and rolling up the strip into a seamless cylinder ($\mathbf{a}_1$ and $\mathbf{a}_2$ are the primitive translations of graphene and L_1 and L_2 are integer numbers). The nanotube is uniquely specified by the pair (L_1, L_2) for $L_1 \geq L_2 \geq 0$. The tubes are termed achiral ("armchair" tubes for $L_1 = L_2$ and "zigzag" tubes for $L_1 \neq L_2 = 0$) and chiral (all other tubes), depending on the presence of a vertical plane of symmetry. The tubes can also be characterized by their radius R and chiral angle θ which is the angle between the chiral vector and the nearest zigzag of carbon-carbon bonds. The nanotube has N carbon pairs in the unit cell. Similar to graphene, where a two-atom unit cell can be mapped onto the entire sheet by use of the two primitive translations vectors, a two-atom unit cell can be mapped onto the entire tube by means of two different primitive screw operations. A screw operation $\{\mathbf{S}|\mathbf{t}\}$ translates the tube at a distance $\mathbf{t}$ along the tube axis and rotates the tube at an angle ϕ around the axis. Any screw operation is a combination of integer numbers of the two different primitive screw operations $\{\mathbf{S}_1|\mathbf{t}_1\}^{l_1}\{\mathbf{S}_2|\mathbf{t}_2\}^{l_2}$. Such an operation coincides a given atom with its equivalent one on the tube. Under a given screw operation, the position vector of an atom in the zeroth unit cell $\mathbf{R}(0\kappa)$ is transformed into the position vector of an equivalent atom $\mathbf{R}(l\kappa)$

which can be written mathematically as $\mathbf{R}(l\kappa) = \{\mathbf{S}_1|\mathbf{t}_1\}^{l_1}\{\mathbf{S}_2|\mathbf{t}_2\}^{l_2}\mathbf{R}(0\kappa) = \mathbf{S}(l)\mathbf{R}(0\kappa) + l_1\mathbf{t}_1 + l_2\mathbf{t}_2$, where $\mathbf{l} \equiv (l_1, l_2)$ is the cell index, $\kappa = 1, 2$ labels the atoms in each cell, and $\mathbf{S}(l) = \mathbf{S}_1^{l_1} \cdot \mathbf{S}_2^{l_2}$. The use of the screw symmetry in atomistic calculations of nanotube properties makes possible large-scale simulations of the physical properties of all tubes of practical interest.[4]

B. The symmetry-adapted force-constant dynamical model

The force-constant lattice dynamical model for nanotubes can be constructed as a Born model of the lattice dynamics based on a two-atom unit cell.[4,22] In the adiabatic approximation, the atomic motion is conveniently decoupled from the electronic one. For small displacements $\mathbf{u}(l\kappa)$ of the atoms from their equilibrium positions $\mathbf{R}(l\kappa)$, it is customary to use the harmonic approximation and represent the atomic Lagrangian as a quadratic form of $\mathbf{u}(l\kappa)$. Using the translational periodicity, rotational boundary condition, and the screw symmetry of the tube, the solution to the equations of motion can be sought in the form

$$u_\alpha(l\kappa) = \frac{1}{\sqrt{M}}\sum_\beta S_{\alpha\beta}(l)e_\beta(\kappa|ql)\exp i[\alpha(l)l + z(l)q - \omega t],$$

(1)

where M is carbon atom mass, $\alpha(\mathbf{l}) = 2\pi(l_1 N_2 - l_2 N_1)/N$, and $z(\mathbf{l}) = (L_1 l_2 - L_2 l_1)/N$; l is the azimuthal quantum number ($l = 0, 1, \ldots, N-1$) and q is the one-dimensional wave vector ($-\pi \leq q < \pi$). Substituting Eq. (1) in the equations of motion, one obtains the system of six homogeneous linear equations

$$\omega^2(ql)e_\alpha(\kappa|ql) = \sum_{\kappa'\beta} D_{\alpha\beta}(\kappa\kappa'|ql)e_\beta(\kappa'|ql),$$

(2)

where the dynamical matrix $D_{\alpha\beta}(\kappa\kappa'|ql)$ is defined as

$$D_{\alpha\beta}(\kappa\kappa'|ql) = \frac{1}{M}\sum_{l'\gamma} \Phi_{\alpha\gamma}(0\kappa, l'\kappa')S_{\gamma\beta}(l')\exp i[\alpha(l')l + z(l')q].$$

(3)

The eigenfrequencies $\omega^2(ql)$ are solutions of the characteristic equation

$$\|D_{\alpha\beta}(\kappa\kappa'|ql) - \omega^2(ql)\delta_{\alpha\beta}\delta_{\kappa\kappa'}\| = 0.$$

(4)

Substituting the solutions $\omega^2(qlj)$ ($j = 1, 2, \ldots, 6$) in Eq. (2), one can obtain the corresponding eigenvectors $e_\alpha(\kappa|qlj)$ ($j = 1, 2, \ldots, 6$). For each q there are $6N$ vibrational eigenmodes (phonons) but the number of the different $\omega^2(qlj)$ can be lesser due to degeneracy. Using Eq. (3) it can be proven that D is Hermitian and therefore $\omega^2(qlj)$ are real and $e_\alpha(\kappa|qlj)$ can be chosen orthonormal.

C. The symmetry-adapted tight-binding model

In the force-constant model of the lattice dynamics, the interatomic interactions are modeled by means of constant parameters. Therefore, the effect of the tube curvature on the

phonon dispersion is included only through the structural parameters of the tube. Moreover, the electron density deformation due to the ionic displacements is most often ignored. On the other hand, the interatomic forces depend on the atomic configuration and the electron density deformation is an important factor modifying the phonon dispersion. An attempt to include both effects can be made within the tight-binding approach.

In the symmetry-adapted NTB model,[20] in view of the translational periodicity, rotational boundary condition, and the screw symmetry, one assumes the one-electron wave function ψ in the form of the following linear combination of basis functions φ (Ref. 20)

$$\psi_{kl}(\mathbf{r}) = \sum_r c_{klr} \varphi_{klr}(\mathbf{r}), \tag{5}$$

where the basis functions φ are represented by use of the atomic orbitals χ as

$$\varphi_{klr}(\mathbf{r}) = \frac{1}{\sqrt{N_c}} \sum_{\mathbf{l}r'} e^{i[\alpha(\mathbf{l})l+z(\mathbf{l})k]} T_{rr'}(\mathbf{l}) \chi_{r'}[\mathbf{R}(\mathbf{l}) - \mathbf{r}]. \tag{6}$$

Here $\chi_r[\mathbf{R}(\mathbf{l})-\mathbf{r}]$ are based on atoms with position vector $\mathbf{R}(\mathbf{l})$ and $r = 1, 2, \ldots, s$ labels the orbitals in the two-atom unit cell ($s=2$ for the π-band TB model and $s=8$ for the all-valence TB model), and N_c is the number of two-atom unit cells in the tube. $T_{rr'}(\mathbf{l})$ are the matrices of the induced representation of the screw symmetry group in the space of the atomic orbitals.

After substitution of Eqs. (6) and (5) in the one-electron Schrödinger equation for the tube, the electronic problem is transformed into the matrix eigenvalue problem

$$\sum_{r'} H_{klrr'} c_{klr'} = E_{kl} \sum_{r'} S_{klrr'} c_{klr'}, \tag{7}$$

where the quantities $H_{klrr'}$ and $S_{klrr'}$ are given by

$$H_{klrr'} = \sum_{\mathbf{l}r''} e^{i[\alpha(\mathbf{l})l+z(\mathbf{l})k]} H_{rr''}(\mathbf{l}) T_{r''r'}(\mathbf{l}) \tag{8}$$

and

$$S_{klrr'} = \sum_{\mathbf{l}r''} e^{i[\alpha(\mathbf{l})l+z(\mathbf{l})k]} S_{rr''}(\mathbf{l}) T_{r''r'}(\mathbf{l}). \tag{9}$$

Here $H_{rr''}(\mathbf{l})$ and $S_{rr''}(\mathbf{l})$ are the matrix elements of the Hamiltonian and the overlap matrix elements between the atomic orbitals $\chi_r[\mathbf{R}(0)-\mathbf{r}]$ and $\chi_{r'}[\mathbf{R}(\mathbf{l})-\mathbf{r}]$.

The set of linear algebraic equations (7) has nontrivial solutions for the coefficients c only for energies E which satisfy the characteristic equation

$$\|H_{klrr'} - E_{kl}S_{klrr'}\| = 0. \tag{10}$$

The solutions of Eq. (10), E_{klm}, are the electronic energy levels ($m = 1, 2, \ldots, s$). The corresponding eigenvectors c_{klmr} are determined from Eq. (7).

For structural relaxation of a nanotube one needs the expressions for the total energy and the forces acting on the atoms. The total energy of a nanotube (per unit cell) is given by

$$E = \sum_{klm}^{occ} E_{klm} + \frac{1}{2} \sum_{ij(i \neq j)} \phi(r_{ij}), \tag{11}$$

where the first term is the band energy E_{BS} (the summation is over all occupied states) and the second term is the repulsive energy E_{rep}, consisting of repulsive pair potentials $\phi(r)$ between pairs of nearest neighbors. The band contribution to the force on the atom with a position vector $\mathbf{R}$ is given by the Hellmann-Feynman theorem

$$\mathbf{F}_{BS} = \sum_{klm}^{occ} \frac{\partial E_{klm}}{\partial \mathbf{R}} = \sum_{klm}^{occ} \sum_{rr'} c_{klr}^* \left(\frac{\partial H_{klrr'}}{\partial \mathbf{R}} - E_{klm} \frac{\partial S_{klrr'}}{\partial \mathbf{R}} \right) c_{klr'}. \tag{12}$$

The repulsive contribution to the force $\mathbf{F}_{rep}$ is the first derivative of the total repulsive energy with respect to the position vector $\mathbf{R}$.

D. The tight-binding approach to the lattice dynamics of carbon nanotubes

The lattice dynamics of nanotubes can be studied by directly calculating the force-constant matrix. In this method, a large enough supercell of the nanotube is considered so that the displacements of atoms in it will not be felt by equivalent atoms in adjacent supercells. This method cannot be applied to all nanotubes because the condition of commensurability of the supercell with the unit cell of the nanotube and the condition for a tractable size of the supercell can be ensured for all achiral tubes but only for a small fraction of chiral tubes. An alternative method consists in the direct calculation of the dynamical matrix. This matrix can be derived within the tight-binding model considering the change in the total energy due to a static lattice deformation (a phonon) (we omit the index ql of e for brevity)

$$\mathbf{u}(\mathbf{l}\kappa) = \mathbf{S}(\mathbf{l})\mathbf{e}(\kappa) e^{i[\alpha(\mathbf{l})l+z(\mathbf{l})q]} + \text{c.c.} \tag{13}$$

The band contribution to this change can be expressed with the change of the one-electron eigenenergies up to second order in perturbation theory. The derivation of the dynamical matrix is too complicated because of the nonorthogonality of the basis functions but it is quite similar to that for finite systems.[12] Here it suffices to provide the final expression for the change of the band energy E_{BS}

$$\begin{aligned} E_{BS} - E_{BS}^{(0)} = &\sum_{kn} \mathbf{c}_{kn}^{+} (\mathbf{H}^{(2)} - E_{kn}\mathbf{S}^{(2)})\mathbf{c}_{kn} - \sum_{kn} \mathbf{c}_{kn}^{+}(\mathbf{H}^{(1)} \\ &- E_{kn}\mathbf{S}^{(1)})\mathbf{c}_{kn}\mathbf{c}_{kn}^{+}\mathbf{S}^{(1)}\mathbf{c}_{kn} + 2\sum_{knn'} (E_{kn} \\ &- E_{k+qn'})^{-1}\mathbf{c}_{kn}^{+}(\mathbf{H}_{0+}^{(1)} - E_{kn}\mathbf{S}_{0+}^{(1)})\mathbf{c}_{k+qn'}\mathbf{c}_{k+qn'}^{+}(\mathbf{H}_{+0}^{(1)} \\ &- E_{kn}\mathbf{S}_{+0}^{(1)})\mathbf{c}_{kn} + 2\sum_{knn'} (E_{kn} - E_{k-qn'})^{-1}\mathbf{c}_{kn}^{+}(\mathbf{H}_{0-}^{(1)} \\ &- E_{kn}\mathbf{S}_{0-}^{(1)})\mathbf{c}_{k-qn'}\mathbf{c}_{k-qn'}^{+}(\mathbf{H}_{-0}^{(1)} - E_{kn}\mathbf{S}_{-0}^{(1)})\mathbf{c}_{kn}. \end{aligned} \tag{14}$$

Here $n \equiv lm$ and $n' \equiv lm'$; the summation is carried out over the entire Brillouin zone and all occupied states (index n)

and empty states (index n'). It can be shown that for $q=0$, the last two sums give finite values except for armchair tubes. $\mathbf{H}^{(1)}$ and $\mathbf{H}^{(2)}$ are first- and second-order changes of $\mathbf{H}$ given by the expressions

$$\mathbf{H}^{(2)} = \frac{1}{2}\sum_{\mathbf{l}'} e^{i[\alpha(\mathbf{l}')l+z(\mathbf{l}')k]}\boldsymbol{\nabla}_\alpha\boldsymbol{\nabla}_\beta\mathbf{H}u_\alpha(\mathbf{0}\kappa\mathbf{l}'\kappa')u_\beta(\mathbf{0}\kappa\mathbf{l}'\kappa'),$$

(15)

$$\mathbf{H}^{(1)} = \sum_{\mathbf{l}'} e^{i[\alpha(\mathbf{l}')l+z(\mathbf{l}')k]}\boldsymbol{\nabla}_\alpha\mathbf{H}u_\alpha(\mathbf{0}\kappa\mathbf{l}'\kappa'),$$

(16)

where $\boldsymbol{\nabla}_\alpha\mathbf{H}$ and $\boldsymbol{\nabla}_\alpha\boldsymbol{\nabla}_\beta\mathbf{H}$ are partial derivatives with respect to $u_\alpha(\mathbf{0}\kappa\mathbf{l}'\kappa') \equiv u_\alpha(\mathbf{0}\kappa) - u_\alpha(\mathbf{l}'\kappa')$ and the exponentials are removed from u_α and u_β. $\mathbf{H}^{(1)}_{0+}$, $\mathbf{H}^{(1)}_{0-}$, $\mathbf{H}^{(1)}_{+0}$, and $\mathbf{H}^{(1)}_{-0}$ are similar to Eqs. (15) and (16) but $\mathbf{u}(\mathbf{0}\kappa\mathbf{l}'\kappa')$ is substituted with $\mathbf{e}^*(\kappa)e^{i[\alpha(\mathbf{l}')l+z(\mathbf{l}')q]} - \mathbf{S}(\mathbf{l}')\mathbf{e}^*(\kappa')$, $\mathbf{e}(\kappa)e^{-i[\alpha(\mathbf{l}')l+z(\mathbf{l}')q]} - \mathbf{S}(\mathbf{l}')\mathbf{e}(\kappa')$, $\mathbf{e}(\kappa) - \mathbf{S}(\mathbf{l}')\mathbf{e}(\kappa')e^{i[\alpha(\mathbf{l}')l+z(\mathbf{l}')q]}$, and $\mathbf{e}^*(\kappa) - \mathbf{S}(\mathbf{l}')\mathbf{e}^*(\kappa')e^{-i[\alpha(\mathbf{l}')l+z(\mathbf{l}')q]}$, respectively. Finally, $\mathbf{S}^{(1)}$, $\mathbf{S}^{(2)}$, $\mathbf{S}^{(1)}_{0+}$, $\mathbf{S}^{(1)}_{0-}$, $\mathbf{S}^{(1)}_{+0}$, and $\mathbf{S}^{(1)}_{-0}$ are defined by expressions similar to those for the corresponding $\mathbf{H}$'s but with $\mathbf{H}$ replaced by the overlap matrix $\mathbf{S}$.

The repulsive energy E_{rep} is expanded in series of $u_\alpha(\mathbf{0}\kappa\mathbf{l}'\kappa')$ up to second power. The dynamical natrix is derived from the expression

$$D_{\alpha\beta}(\kappa\kappa'|ql) = \frac{1}{M}\frac{\partial^2(E_{\text{BS}}+E_{\text{rep}})}{\partial e_\alpha(\kappa|ql)\partial e_\beta(\kappa'|ql)}.$$

(17)

The phonon eigenvalues and eigenvectors are then obtained as solutions of Eq. (2).

III. RESULTS AND DISCUSSION

A. Phonon dispersion of graphene

We relaxed the atomic structure of graphene within the NTB model using over 2000 k points in the irreducible Brillouin zone. The relaxed lattice constant was 2.458 Å. The large number of k points was not necessary for the structural relaxation but it was crucial for achieving convergence of the phonon frequencies within 1 cm^{-1}. The reason for the slow convergence of the latter can be found in the presence of crossing electronic bands at the Fermi energy at the K and K' points of the Brillouin zone. For each pair of electronic states, belonging to these two bands and having very small energy difference, the last two terms in Eq. (14) become very large. However, this does not cause any divergence problems because the total contribution from the k points around the K and K' points is finite.

The calculation of the phonon dispersion of graphene was performed using the dynamical matrix (17). In this approach, one calculates the electronic band structure for the unit cell only and uses only the electronic eigenenergies and eigenfunctions for the unit cell atoms in the estimation of the matrix elements and the summation over the Brillouin zone. Therefore, phonons in any point of the Brillouin zone can be calculated with the same computational effort. In this respect, this approach has an advantage over the supercell
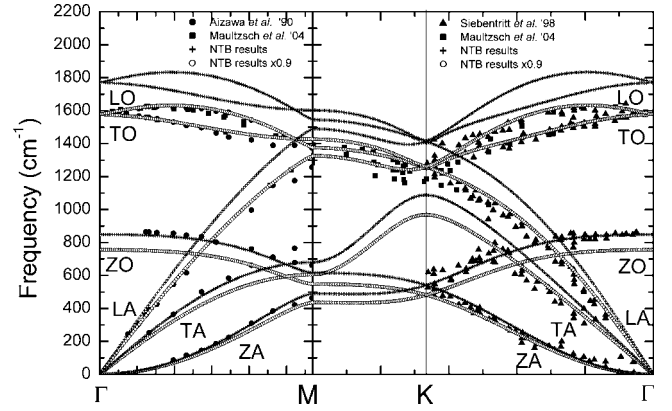

FIG. 1. The calculated phonon dispersion of graphene within the NTB model (crosses) in comparison with available experimental data (solid symbols). The phonon curves, downshifted by a factor of 0.9, are shown by empty circles. The discontinuous first derivative of the LO branch at the Γ point and the TO branch at the K point are signatures of Kohn anomaly at these points (Ref. 26).

method where only phonons with wavelength commensurate with the supercell can be calculated.[15] On the other hand, in the dynamical matrix method, one has to sum over an infinite number of unoccupied electronic bands and the use of a finite number of such bands can affect the final results.

The obtained phonon dispersion of graphene in shown with crosses in Fig. 1 in comparison with available experimental data.[23–25] It is clear, that while there is an overall good agreement for the out-of-plane phonons (ZA and ZO), there is a systematical overestimation of the in-plane ones of bond-stretching character (TA, LA, TO, and LO) of about 11%. This overestimation can be reduced by downshifting the mentioned phonon branches by a factor of 0.9. The scaled branches, shown by empty circles, agree quite well with the experimental points and the *ab initio* results.[15,25] Since we are interested in the prediction of the bond-stretching modes, we compare the various data in the high-frequency region. The values of the in-plane phonon frequencies at points Γ, M, and K are given in Table I. At the Γ point, the experiment yields 1565, 1577, and 1583 cm^{-1}, while theory predicts values of 1595 cm^{-1} (Ref. 15), 1581 cm^{-1} (Ref. 25), and 1582 cm^{-1} (here). All data exhibit characteristic "overbending" of the LO phonon branch along ΓM and ΓK. The experimental overbending, understood as the highest LO frequency with respect the Γ-point one, is about 30 cm^{-1}. Theory gives overbending of ≈ 40 cm^{-1} (Ref. 15), ≈ 35 cm^{-1} (Ref. 25), and ≈ 54 cm^{-1} (this work). Largest deviations between theory and experiment are present for the TO branches around the K point. There is no measurement of the TO frequency at the K point and the cubic spline extrapolation yields a splitting between LO(K) and TO(K) phonons of 70 cm^{-1} (Ref. 25). The predicted values for this splitting has a large spread: 140 cm^{-1} (Ref. 15), 80 cm^{-1} (Ref. 25), and vanishingly small (here).

The discrepancy between the various estimations of the LO(K) − TO(K) splitting can be explained in terms of a Kohn anomaly originating from strong electron-phonon interactions. The discontinuous first derivative with respect to the wave vector of the LO branch at the Γ point and the TO

TABLE I. Calculated phonon frequencies in several points of the Brillouin zone of graphene in comparison with available experimental and computational data.

Phonon Branch	Point	Expt.[a]	Calc.[a]	Calc.[b]	Calc. here ($\times 0.9$)
TO	Γ	1565	1581	1595	1582
	M	1390	1425	1442	1430
	K	1265[c]	1300	1370	1262
LO	Γ	1577/1583	1581/1582	1595	1582
	M	1323	1350	1380	1384
	K	1194	1220	1240	1265
LA	Γ	0	0	0	0
	M	1290	1315	1339	1324
	K	1194	1220	1240	1262

[a]Reference 25.
[b]Reference 15.
[c]Obtained from a cubic spline extrapolation (Ref. 25).

branch at the K point, clearly seen in Fig. 1, is a manifestation of such anomaly.[26] Since this effect arises from electrons close to the Fermi energy, the anomalous behavior is strongly suppressed with the increase of the temperature. The *ab initio* models use finite temperature population of the electronic levels[15,26,17,18] which results in a higher TO phonon branch at the K point compared to the NTB one, computed at zero temperature. We have not studied the effect of finite temperature on this phonon branch because this goes beyond the scope of this paper. However, we performed all calculations of the RBM and the G-band phonons of nanotubes in the next sections at temperature of 300 K. Technically, this is done by using partial occupancy of the electronic bands in Eq. (14) given by the Fermi-Dirac distribution function.

B. Phonon dispersion of carbon nanotubes

The nanotube structure of all 300 nanotubes in the radius range from 2 to 12 Å was relaxed as described in Ref. 20. The phonon dispersion of these tubes was then calculated for the relaxed tube structure in the one-dimensional Brillouin zone of the tubes. The convergence of the phonon frequencies up to 1 cm^{-1} in semiconducting tubes, tiny-gap tubes, and most of the branches of armchair tubes was achieved with a number of k points given by the expression $5000/\sqrt{N}$. The obtained phonon dispersion for three narrow tubes (11,0), (12,0), and (7,7) with small N is shown in Fig. 2. The comparison between the behavior of the phonon branches of these tubes reveals anomalous behavior of certain phonon branches in tubes (12,0) and (7,7) due to strong electron-phonon interactions. The tube (12,0) is metallic according to the πTB picture but is a tiny-gap semiconductor according to the NTB model.[20] However, the tiny gap is not sufficient for removing the anomalous branch softening and, in the study of this anomaly, we shall refer to both armchair and tiny-gap tubes as "metallic" ones.

In order to reveal the nature of the anomalous behavior in metallic tubes, we assume k-independent numerator in Eq.
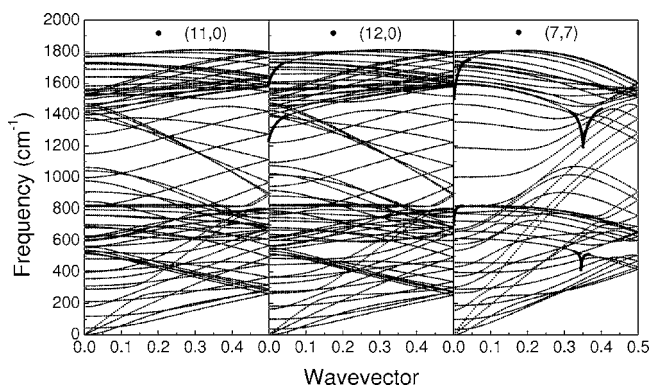

FIG. 2. The phonon dispersion of three narrow nanotubes (11,0), (12,0), and (7,7) calculated within the NTB model. Certain branches of tubes (12,0) and (7,7) show Kohn anomaly at the zone center and at k points inside the Brillouin zone (bold lines) which can be attributed to strong electron-phonon interactions.

(14). It is then clear that the strong coupling of two electrons with wave vectors k_1 and k_2 with length k_F at the Fermi surface by a phonon with a wave vector $q=k_2-k_1$ leads to small values of the denominator, divergence of the dynamical matrix, and anomalous softening of certain phonon branches, which is known as the Kohn anomaly. In nanotubes, there are two possible cases: (a) $k_2=k_1=k_F$ and therefore $q=0$, and (b) $k_2=-k_1=k_F$ and $q=2k_F$ (up to a reciprocal lattice vector).

Two branches of tube (12,0) soften around the zone center. For our study it is important that the longitudinal A_1 phonon of the G band (or, briefly, A_1^{LO} phonon) of the higher-frequency branch shows pronounced softening. The presence of a tiny gap ensures, however, the convergence of the zone-center phonons of these branches with the increase of the number of the k points.

The phonon dispersion of the armchair tube (7,7) shows logarithmic anomalies at the Γ point and in two mirror points inside the Brillouin zone. For tube (7,7), $k_F=0.325$ (in units of 2π) and Kohn anomalies are observed at $q=0$ (the A_1^{LO} phonon and a counterphase radial A_1 phonon) and $q=2k_F=2\times0.325=0.65$ or, reduced to the first Brillouin zone $q=0.35$ (a circumferential phonon and a radial phonon, both belonging to B_1 branches) (see Figs. 2 and 3). At low temperature, the Kohn anomalies at $q=0$ can be the reason for relaxation of the nanotube to a distorted structure with preservation of the unit cell, while the anomalies at $q=0.35$ can give rise to incommensurate distorted structures. The type of the distorted structures depends on the competition of the soft phonons with temperature.[18]

Among the RBM and the G-band phonons, only the A_1^{LO} phonons of metallic tubes show Kohn anomaly. The simplest way to suppress the Kohn anomaly and to simulate a more realistic situation is by introducing thermal population of the electronic bands in metallic tubes: close to the crossing of the bands at the Fermi energy in armchair tubes and around the gap in tiny-gap semiconductors. The use of rather large and unrealistic broadening factors $\sim$0.1 eV ($\sim$1200 K) yields higher A_1^{LO} frequencies than the observed ones.[15] We use a realistic broadening factor of 0.025 eV ($\approx$300 K) (Ref.
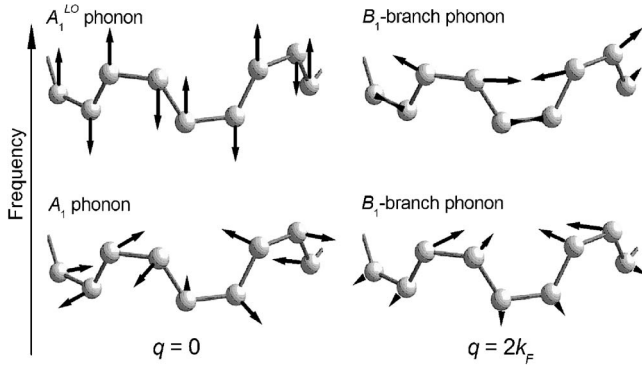
FIG. 3. The eigenvectors of the soft phonons at points $q=0$ and $q=2k_F$ of nanotube (7,7) calculated within the NTB model. These phonons are either A_1 ones, or belong to B_1 phonon branches. The upper figures correspond to higher phonon frequency and vice versa, as indicated by the side arrow.
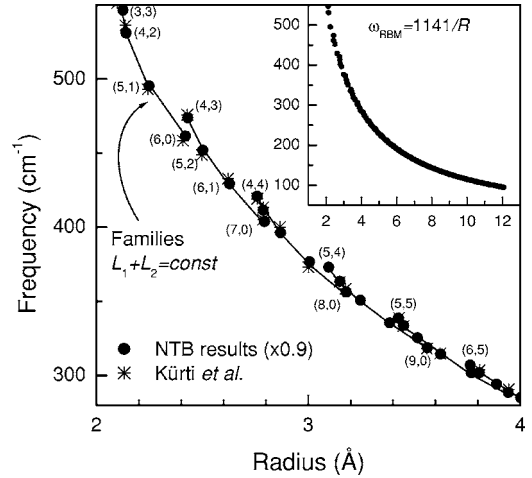

FIG. 4. The RBM frequency of all nanotubes in the radius range from 2 to 12 Å, obtained by fitting Eq. (18) to the NTB results, reduced by a factor of 0.9. The data were fitted by the power law $1141/R$ (inset). The RBM frequencies in the small-radius region are shown in comparison with available *ab initio* results (crosses) (Ref. 27).

18) in all calculations of the RBM and the G-band modes in the following sections. The finite temperature simulation increases the A_1^{LO} phonons frequency of tiny-gap semiconductors by about 80 cm^{-1}. However, this procedure does not remove the logarithmic divergence for armchair tubes in the NTB model. This can be done in more sophisticated approaches where the electronic screening is accounted for.[18]

Tubes with large N have large number of optical phonon branches which are almost disperseless and cover densely the graph. In this case, the phonon density of states would be a more suitable quantity for representation of the vibrational eigenstates. The calculation of this quantity goes outside the scope of this paper.

C. Radial-breathing mode

Next, we turn our attention to the RBM of nanotubes because it gives most intense Raman signal and can be used for nanotube characterization by Raman scattering spectroscopy. The atomic motion in this mode is, within a few degrees, a uniform radial one, the departure from pure radiality being larger for narrow tubes. Although normaly one can assume a pure radial motion for the RBM, this assumption has to be used with care because it can bring about large errors in some cases, e.g., in the Raman intensity simulations.

The calculated RBM frequencies of all 300 nanotubes in the radius range from 2 to 12 Å were downshifted by 0.9 for best agreement with available *ab initio* ones for narrow tubes.[27] Again as with the phonon dispersion of graphene, the best downshift factor was found to be ≈ 0.9. The downshifted RBM frequencies ω_{RBM} were fitted by the chirality-dependent expression

$$\omega_{RBM} = \frac{a_2}{R^{n_2}} + \frac{a_3}{R^{n_3}} \cos 3\theta, \quad (18)$$

where a_2, a_3, n_2, and n_3 are fitting parameters. The best fit with rms accuracy of 1 cm^{-1} is illustrated in Fig. 4 for $R < 5.5$ Å and the inset of Fig. 4 for $R < 12$ Å, and the best fit parameters are provided in Table II. The adding of more

power terms to the fitting expression did not improve much the fit to the calculated data.

The discrete atomic structure of the tubes gives rise to a chirality dependence of the RBM frequency, especially pronounced for narrow tubes, as seen in Fig. 4. The data show well-expressed "family" patterns with $L_1+L_2=$const. The end points of each family are those of zigzag tubes (lower frequency end) and armchair (or close to armchair type) tubes (higher-frequency end). It is interesting to note that all data lie in a strip with the points for zigzag tubes at the lower boundary and the points for armchair tubes at the upper boundary. In other words, close-to-armchair tubes have slightly higher RBM frequencies than those for close-to-zigzag tubes with similar radii. Similar behavior have the points of the *ab initio* data for narrow tubes (crosses in Fig. 4).[27]

Finally, as it is customary, the calculated RBM frequencies were fitted by a much simpler and chirality-independent power law a/R where $a=1141$ cm^{-1} Å (see Fig. 4, inset). This value of a is in agreement with the *ab initio* estimates of 1160 (Ref. 14), 1170 (Ref. 27), and 1144 (Ref. 15).

D. G-band modes

We calculated the G-band modes frequencies for all 300 nanotubes in the radius range from 2 to 12 Å. The eigenvectors correspond with accuracy of several degrees to circumferential or axial atomic displacement. This allows us to refer to these modes as transverse and longitudinal (TO and LO). The obtained G-band frequencies were downshifted by a factor of 0.9 and all but the $A_1^{LO}(M)$ ones of metallic (M) tubes were fitted by use of the expression

$$\omega_{G\ band} = a_0 + \frac{a_1}{R^{n_1}} + \frac{a_2}{R^{n_2}} + \frac{a_3}{R^{n_3}} \cos 3\theta, \quad (19)$$

where a_0, a_1, a_2, a_3, n_1, n_2, and n_3 are fitting parameters, a_0 is the same for all G-band phonons, and a_1 and n_1 are set to

TABLE II. Fitting parameters of Eq. (18) for the RBM and all G-band modes with the exception of the A_1^{LO} ones of metallic tubes. For the RBM, $a_0=0$, while the value $a_0=1582$ cm^{-1} is the same for all G-band modes.

Mode	a_1	n_1	a_2	n_2	a_3	n_3
RBM	0	0	1300.28	1.00692	−149.83	2.34283
A_1(LO)	−386.90	1.68479	196.12	1.01650	−369.46	2.81735
A_1(TO)	0	0	−768.09	2.16246	53.66	1.49888
E_1(LO)	0	0	−641.98	2.47920	−391.14	2.57209
E_1(TO)	−833.31	1.64039	457.86	1.06488	−700.32	3.11029
E_2(LO)	0	0	−690.21	1.99125	−818.61	2.56233
E_2(TO)	−1567.81	1.76031	740.95	1.05585	−826.76	2.88743

zero for the A_1^{TO}, E_1^{LO}, and E_2^{LO} phonons. The obtained best fit parameters are given in Table II. For the sake of clarity, we present in Fig. 5 only the results of the fittings. The fits have rms accuracy below 2 cm^{-1} with larger deviations for narrower tubes. The calculated data for the $A_1^{LO}(M)$ frequencies of tiny-gap semiconducting tubes could not be fitted by means of Eq. (18). In fact, the smearing of the Kohn anomaly and the upshift of the softened mode frequency depends crucially on the thermal population of the electronic states close to the Fermi energy through an exponential factor. Therefore, we tried fitting the latter data with the combination of exponentials

$$\omega_M = a_0 + a_1 e^{-b_1 R} + a_2 e^{-b_2 R} \cos 3\theta \qquad (20)$$

and obtained satisfactory r.m.s. accuracy of the same order as for the other G-band modes (see Fig. 5). Here, $a_0=1582$ cm^{-1}, $a_1=-433.08$ cm^{-1}, $b_1=0.30037$ Å, $a_2=340.45$ cm^{-1}, and $b_2=0.64747$ Å. The data for armchair
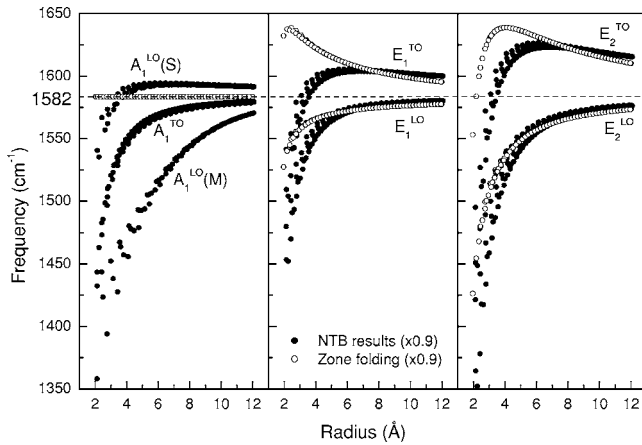

FIG. 5. The G-band mode frequencies for all nanotubes in the radius range from 2 to 12 Å obtained by fitting Eqs. (19) and (20) to the NTB results, reduced by a factor of 0.9. The corresponding frequencies, obtained by zone-folding of the NTB phonon dispersion of graphene, are provided for comparison. Major differences between both sets of data are observed for $R<6$ Å. All curves tend to the optical phonon frequency of graphene of 1582 cm^{-1} (dashed line) in the large-radius limit. The A_1^{LO} mode frequency of metallic tubes exhibits large softening due to strong electron-phonon interactions.

tubes were not included in the fitting because of the inherent divergence of the $A_1^{LO}(M)$ frequency but we suppose that Eq. (20) should give a fair prediction for this case as well and the points for armchair tubes were added to the $A_1^{LO}(M)$ strip in Fig. 5.

For large radii, the derived frequencies of all six G-band modes tend to the frequency of the in-plane optical mode of graphite with measured value of 1582 cm^{-1}. For small radii, there is a well-expressed curvature-induced softening of the frequencies of all modes and additional softening of the $A_1^{LO}(M)$ strip because of strong electron-phonon interactions. For moderate- and large-radius tubes, the inequality $A_1^{LO}(M)<E_2^{TO}<E_1^{LO}\approx A_1^{TO}<A_1^{LO}<E_1^{TO}<E_2^{TO}$ holds for the frequencies of the six modes. This behavior agrees with the *ab initio* results[15] except for the larger $E_1^{TO}-E_1^{LO}$ and $E_2^{TO}-E_2^{LO}$ splitting. For example, for tube (12,6), we obtain values of 31 and 64 cm^{-1}, which are almost twice larger than the *ab initio* ones 15 and 48 cm^{-1}, obviously due to the larger overbending of the LO phonon branch of graphene predicted here. The same is true for the downshift of the A_1^{LO} frequency of metallic tubes relative to the optical phonon frequency of graphene, e.g., the NTB value of 63 cm^{-1} for the tiny-gap semiconductor (12,6) is larger than the *ab initio* one of 48 cm^{-1} (derived from the fitting expression $300/R$ to *ab initio* data) and the experimental one of 51 cm^{-1} (derived from the empirical expression $1987.5/R$).[25] On the other hand, the $A_1^{LO}-A_1^{TO}$ splitting of 32 cm^{-1} for the semiconducting tube (10,0) is smaller than the *ab initio* result of about 40 cm^{-1}.

The effect of the tube curvature on the radius dependence of the G-band modes can be seen in comparison with the zone-folding results (see Fig. 5). The A_1 modes are zone-center ones in graphene and they do not change upon zone folding. Therefore, the zone-folded A_1 mode frequencies lie on a horizontal line. The A_1 NTB data is an almost horizontal line down to $R\approx 6$ Å and a downward going curve for $R<6$ Å. Therefore, the curvature effects on the A_1 are essential below 6 Å and, in this radius range, calculations based on the relaxed tube structure have to be carried out instead of using the zone-folded results. The E_1 and E_2 modes of nanotubes originate from the inside of the Brillouin zone of graphene. For this reason, the zone-folding method yields radius dependence of these tube modes for the NTB data but the zone-folding data do not have the profound chirality dependence of the NTB data. Again, we notice that while the
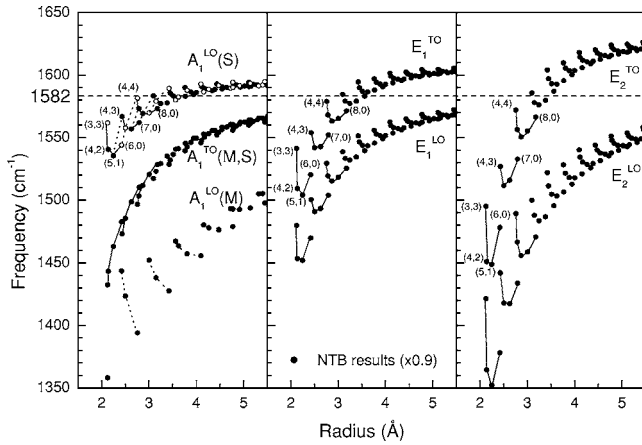
FIG. 6. The small-radius region of the graph in Fig. 5 showing the strong chirality dependence of the G-band mode frequencies (solid circles). The empty circles on the left panel only mark the positions of the $A_1^{LO}(M)$ frequencies as obtained from Eq. (19). The bottom strip of points on the same panel gives the $A_1^{LO}(M)$ frequencies derived by fitting Eq. (20) to the NTB results. The circles on all panels show characteristic family patterns for L_1+L_2=const and $2L_1+L_2$=const illustrated with solid and dotted lines, respectively.

zone-folding method gives acceptable results for radii larger than ≈ 6 Å, this method is no longer reliable for smaller radii.

The discrete atomic structure begins to manisfest itself through the chirality dependence of the G-band modes frequencies. Similarly to the RBM data, the points here show clear pattern arrangement for L_1+L_2=const but also for $2L_1+L_2$=const. This behavior is best seen in the small-radius region, as shown in Fig. 6. Again as for the RBM, the obtained points lie on strips, which become wider for smaller radii. The points for close-to-armchair tubes are situated at the upper boundaries of the strips and the points for close-to-zigzag tubes are at the lower boundaries. An exclusion to this are the A_1^{TO} data where the close-to-zigzag tube frequencies are higher than those of the close-to-armchair tubes. This peculiar behavior can be observed for the data from phenomenological force-constant calculations.[4] In the latter case, two different assumptions for the tube structure were made: (1) equal bond-length and equal-bond-angle structure and (2) rolled-up tube structure (see, Sec. II A). Therefore, there is no evidence for correlation of the mentioned behavior of the A_1^{TO} data with the bond lengths and bond angles in tubes. Obviously, this behavior is mainly due to the nonplanarity of the three adjacent bonds and the resulting softening of the bond-stretching and angle-bending force constants.

The curvature-induced change of the A_1 modes has been observed in the case of isolated nanotubes.[5] The limited radius distribution of the tubes allowed to conclude that (1) the A_1 modes frequencies are chirality independent, (2) the A_1 data lie on two subbands: a higher-frequency nondispersive one G^+ of the A_1^{LO} mode and a lower-frequency dispersive one G^- of the A_1^{TO} mode, (3) the G^- subband has a higher-frequency component due to semiconducting tubes and a lower-frequency component due to metallic tubes, and (4) both G^+ and G^- subbands contain points of metallic and semiconducting tubes. Our extended study reveals that both

subbands soften at small radii though to a different extent. According to the calculated data for the A_1 modes of all considered tubes, we can conclude that (1) the G^+ strip should be due only to A_1^{LO} modes of semiconducting tubes with no contribution from metallic tubes (see also Ref. 15), (2) the semiconducting G^- subband should contain contributions from A_1^{TO} modes of both semiconducting and metallic tubes, and (3) the metallic G^- subband should arise from A_1^{LO} phonons of metallic tubes. The softening of the latter modes depends on temperature and this effect requires additional study. The major and quite puzzling discrepancy between theory and experiment is the observation of lines due to metallic tubes in the G^+ subband and the assignment of the lower-frequency component of the G^- subband to A_1^{TO} phonons, which is in contradiction with the theoretical predictions of strong-electron–A_1^{LO} phonon interactions in metallic tubes accompanied by drastic softening of the A_1^{LO} phonon frequencies. In order to resolve the puzzling disagreement of the determined subband character with the observations, precise experimental data and more sophisticated computer simulations are necessary.

IV. CONCLUSIONS

In this paper, we show that a semiquantitative description of the phonon dispersion of the carbon nanotubes can be achieved by using the dynamical matrix method within the tight-binding electronic band-structure picture of the tubes. The symmetry-adapted scheme, which is incorporated in the tight-binding model, allows for handling practically all currently produced carbon nanotubes.

The obtained data for the frequency of the RBM and the G-band modes were found to show curvature-induced softening with the decrease of the tube radius as well as well-expressed chirality dependence and clearly seen family patterns. Major differences between the NTB and zone-folding results are observed for radii smaller than ≈ 6 Å that can be considered as the limiting tube radius for reliability of the zone-folding predictions. We found that the NTB eigenvectors of the RBM and the G-band modes correspond within several degrees to predominantly radial, axial, and circumferential atomic motion.

The strong-electron–A_1^{LO} phonon interaction in metallic nanotubes leads to Kohn anomalies in the phonon dispersion. In particular, the frequency of the A_1^{LO} phonons softens below that of the A_1^{TO} ones and therefore the A_1^{LO} phonons should give rise to a lower-frequency component of the G^- subband of the Raman spectra. This result is in disagreement with the wide-spread assignment of this component to A_1^{TO} phonons of metallic nanotubes.

*Permanent address: Faculty of Physics, University of Sofia, BG-1164 Sofia, Bulgaria.

[1] *Carbon Nanotubes: Synthesis, Structure, Properties, and Applications*, edited by M. S. Dresselhaus, G. Dresselhaus, and Ph. Avouris (Springer-Verlag, Berlin, 2001).

[2] R. A. Jishi, L. Venkataraman, M. S. Dresselhaus, and G. Dresselhaus, Chem. Phys. Lett. **209**, 77 (1993).

[3] R. Saito, T. Takeya, T. Kimura, G. Dresselhaus, and M. S. Dresselhaus, Phys. Rev. B **57**, 4145 (1998).

[4] V. N. Popov, V. E. Van Doren, and M. Balkanski, Phys. Rev. B **59**, 8355 (1999).

[5] A. Jorio, A. G. Souza Filho, G. Dresselhaus, M. S. Dresselhaus, A. K. Swan, M. S. Ünlü, B. Goldberg, M. A. Pimenta, J. H. Hafner, C. M. Lieber, and R. Saito, Phys. Rev. B **65**, 155412 (2002).

[6] A. Kasuya, Y. Sasaki, Y. Saito, K. Tohji, and Y. Nishina, Phys. Rev. Lett. **78**, 4434 (1997).

[7] S. Reich, C. Thomsen, G. S. Duesberg, and S. Roth, Phys. Rev. B **63**, 041401(R) (2001).

[8] R. Saito, A. Jorio, J. H. Hafner, C. M. Lieber, M. Hunter, T. McClure, G. Dresselhaus, and M. S. Dresselhaus, Phys. Rev. B **64**, 085312 (2002).

[9] S. D. M. Brown, A. Jorio, P. Corio, M. S. Dresselhaus, G. Dresselhaus, R. Saito, and K. Kneipp, Phys. Rev. B **63**, 155414 (2001).

[10] J. Maultzsch, S. Reich, and C. Thomsen, Phys. Rev. B **65**, 233402 (2002).

[11] J. Yu, R. K. Kalia, and P. Vashishta, J. Chem. Phys. **103**, 6697 (1995).

[12] M. Menon, E. Richter, and K. Subbaswamy, J. Chem. Phys. **104**, 5875 (1996).

[13] D. Kahn and J. P. Lu, Phys. Rev. B **60**, 6535 (1999).

[14] D. Sánchez-Portal, E. Artacho, J. M. Soler, A. Rubio, and P. Ordejón, Phys. Rev. B **59**, 12 678 (1999).

[15] O. Dubay and G. Kresse, Phys. Rev. B **67**, 035401 (2003).

[16] L.-H. Ye, B.-G. Liu, D.-S. Wang, and R. Han, Phys. Rev. B **69**, 235409 (2004).

[17] K.-P. Bohnen, R. Heid, H. J. Liu, and C. T. Chan, Phys. Rev. Lett. **93**, 245501 (2004).

[18] D. Connétable, G.-M. Rignanese, J.-C. Charlier, and X. Blase, Phys. Rev. Lett. **94**, 015503 (2005).

[19] C. T. White, D. H. Robertson, and J. W. Mintmire, Phys. Rev. B **47**, R5485 (1993).

[20] V. N. Popov, New J. Phys. **6**, 17 (2004).

[21] V. N. Popov and L. Henrard, Phys. Rev. B **70**, 115407 (2004).

[22] V. N. Popov, V. E. Van Doren, and M. Balkanski, Phys. Rev. B **61**, 3078 (2000).

[23] T. Aizawa, R. Souda, S. Otani, Y. Ishizawa, and C. Oshima, Phys. Rev. B **42**, 11 469 (1990).

[24] S. Siebentritt, R. Pues, K.-H. Rieder, and A. M. Shikin, Phys. Rev. B **55**, 7927 (1997).

[25] J. Maultzsch, S. Reich, C. Thomsen, H. Requardt, and P. Ordejón, Phys. Rev. Lett. **92**, 075501 (2004).

[26] S. Piscanec, M. Lazzeri, F. Mauri, A. C. Ferrari, and J. Robertson, Phys. Rev. Lett. **93**, 185503 (2004).

[27] J. Kürti, V. Zólyomi, M. Kertesz, and G. Sun, New J. Phys. **5**, 125 (2003).